Further evidence for energy landscape flattening in the superionic argyrodites $Li_{6+x}P_{1-x}M_xS_5I$ (M = Si, Ge, Sn)

Saneyuki Ohno[a,b], Bianca Helm [a,b], Till Fuchs[a,b], Georg Dewald[a,b], Marvin A. Kraft[a,b],

Sean P. Culver[a,b], Anatoliy Senyshyn[c], Wolfgang G. Zeier*[a,b]

[a]*Institute of Physical Chemistry, Justus-Liebig-University Giessen, Heinrich-Buff-Ring 17, D-35392 Giessen, Germany.*

[b]*Center for Materials Research (LaMa), Justus-Liebig-University Giessen, Heinrich-Buff-Ring 16, D-35392 Giessen, Germany.*

[c]*Heinz Maier-Leibnitz Zentrum, Technische Universität München, 85748 Garching, Germany*

Abstract

All-solid-state batteries are promising candidates for next-generation energy storage devices. Although the list of candidate materials for solid electrolytes has grown in the past decade, there are still many open questions concerning the mechanisms behind ionic migration in materials. In particular, the lithium thiophosphate family of materials has shown very promising properties for solid-state battery applications. Recently, the Ge-substituted Li_6PS_5I argyrodite was shown to be a very fast Li-ion conductor, despite the poor ionic conductivity of the unsubstituted Li_6PS_5I. Therein, the conductivity was enhanced by over three orders of magnitude due to the emergence of I^-/S^{2-} exchange, *i.e.* site-disorder, which led to a sudden decrease of the activation barrier with a concurrent flattening of the energy landscapes. Inspired by this work, two series of elemental substitutions in $Li_{6+x}P_{1-x}M_xS_5I$ (M = Si and Sn) were investigated in this study and compared to the Ge-analogue. A sharp reduction in the activation energy was observed at the same M^{4+}/P^{5+} composition as previously found in the Ge-analogue, suggesting a more general mechanism at play. Furthermore, structural analyses with X-ray and neutron diffraction indicate that similar changes in the Li-sublattice occur despite a significant variation in the size of the substituents, suggesting that in the argyrodites, the lithium substructure is most likely influenced by the occurring $Li^+ - Li^+$ interactions. This work provides further evidence that the energy landscape of ionic conductors can be tailored by inducing local disorder.

1. Introduction

Over the last three decades, Li-ion batteries have become the leading energy storage technology for consumer electronics, demonstrating consistent improvements in electrochemical performance stemming from both materials and engineering advancements. However, the current Li-ion battery architecture is approaching its physicochemical limit in terms of energy density.[1] One promising alternative for the next generation of batteries is the all-solid-state battery, which may enable further enhancements in the energy density, if a Li-metal anode can be used. Moreover, by replacing the combustible, conventional liquid electrolytes, the risk of thermal runaway can also be eliminated. Although there are still remaining challenges to make all-solid-state batteries commercially viable,[2-13] performances surpassing the conventional Li-ion batteries have already been demonstrated.[14] As a role of electrolytes, a fast cation conduction with negligible electronic transport is a requirement for the solid electrolytes. Accordingly, a variety of superionic conductors have already been developed and, especially the class of lithium-thiophosphates, *e.g.* $Li_{10}GeP_2S_{12}$,[14–22] the thio-LISICONS,[23–25] the lithium thiophosphate glasses[26–29] and the Li-argyrodites Li_6PS_5X (X = Cl, Br)[30–37] exhibit exceptionally high ionic conductivities.

Nevertheless, to further improve the performance of solid electrolytes and increase the list of candidate materials, the mechanisms behind ion migration in solids must be elucidated. For instance, aliovalent substitutions are typically used to increase ionic conductivity by changing charge carrier densities. Furthermore, recent studies have highlighted the correlation between lattice dynamics and ion migration that can also be used to improve ionic transport,[32,38–40] indeed explaining why thiophosphate-based electrolytes exhibit these low migration barriers for ionic motion in the first place. In addition, the importance of the local structure and local diffusion pathways on ionic transport has also been shown.[41–43] Regarding the lithium argyrodites, significant enhancements in the ionic conductivity have been achieved through aliovalent substitution and the introduction of disorder within $Li_{6+x}P_{1−x}Ge_xS_5I$.[31]

While the Li_6PS_5X (X = Cl, Br) compositions are Li-superionic conductors at room temperature ($\sigma = 1 − 2 \cdot 10^{-3}$ S cm^{-1}), the I-analogue Li_6PS_5I is known to possess three orders of magnitude lower Li-ion conductivity ($\sigma \sim 10^{-6}$ S cm^{-1}), despite its formally identical crystal structure to the Cl- and Br-analogues. At room temperature, a fully ordered Li-argyrodite Li_6PS_5X (see Figure 1a) crystallizes in a cubic structure type ($F\overline{4}3m$), in which the halide anions $X^−$ form a face-centered cubic lattice (Wyckoff 4a) with the $PS_4^{3−}$ tetrahedra on the octahedral sites (P on Wyckoff 4b) and free $S^{2−}$ anions in half of the tetrahedral sites (Wyckoff 4d). With respect to

the Li-ions, there are two possible crystallographic sites (*i.e.* Wyckoff 24*g* and 48*h*) forming a cage-like structure around the free S^{2-}, thereby enabling three unique migration paths for Li^+ diffusion: 48*h* – 24*g* – 48*h* (doublet jump), 48*h* – 48*h* within the cage (*intra*-cage jump), and 48*h* – 48*h* between the cages (*inter*-cage jump). Previous elemental substitutions that have been performed include substitutions on the halide position,[32] the free sulfur site[44] and the $(P_{1-x}M_x)S_4^{(3+x)-}$ units.[31,33] In the Cl- and Br-analogues, a significant amount of site-disorder between the X^- and the free S^{2-} has been observed, whereas in the I-analogue this site-disorder vanishes, as the ionic radius of I^- is too large to allow for occupancy on the S^{2-} site (ionic radii: Cl^- (1.81 Å), Br^- (1.96 Å), I^- (2.20 Å), and S^{2-} (1.84 Å))[45]. Notably, it has been shown that the lack of site-disorder leads to higher activation barriers, given that the site-disorder facilitates the *inter*-cage jump, which represents the rate-limiting (bottleneck) jump process.[30,32,46] Schematically shown in Figure 1b, the X^- site is adjacent to the bottleneck pathway of the Li^+ jumps. If site-disorder is present, a reduction of the migration barrier is usually observed (Figure 1c).[30,32,46] Recently, the substitution of $Li_{6+x}P_{1-x}Ge_xS_5I$ with Ge^{4+} further corroborated the influence of this beneficial site-disorder on the transport.[43] With increasing Ge^{4+}/Li^+ fraction, the overall lattice volume increases and induces site-disorder, thereby flattening the energy landscape (see Figure 1c) and enhancing the ionic conductivity in $Li_{6+x}P_{1-x}Ge_xS_5I$ drastically.[31]

Inspired by the observed drop in the activation barrier upon Ge substitution in $Li_{6+x}P_{1-x}Ge_xS_5I$, here we explore the aliovalent substitution of the lithium superionic argyrodites $Li_{6+x}P_{1-x}M_xS_5I$. Using M = Si and Sn and increasing the M^{4+}/P^{5+} ratio, we explore the structural changes and influences on the ionic transport properties, in relation to the effects found for $Li_{6+x}P_{1-x}Ge_xS_5I$. Using a combination of Rietveld refinements against X-ray diffraction and neutron diffraction data, as well as electrochemical impedance spectroscopy, we find that the overall lattice volume increases due to the larger ionic radii, which also affects the respective solubility limits. However, the neutron diffraction data suggest that the underlying lithium substructure is mostly influenced by the charge carrier density, rather than the lattice volume changes. Lastly, the series of $Li_{6+x}P_{1-x}Si_xS_5I$ solid solutions exhibits a large drop in the activation barrier, which is associated with a flattening of the energy landscape upon activation of the local site-disorder between S^{2-} and I^-. This work demonstrates that lithium-lithium interactions, along with the influence of carrier density on the lithium substructure, are important considerations for the enhancement of ionic conductor transport properties. Additionally, it provides further evidence that local disorder can severely affect the local diffusion behavior and the potential energy landscape in the lithium conducting argyrodites.
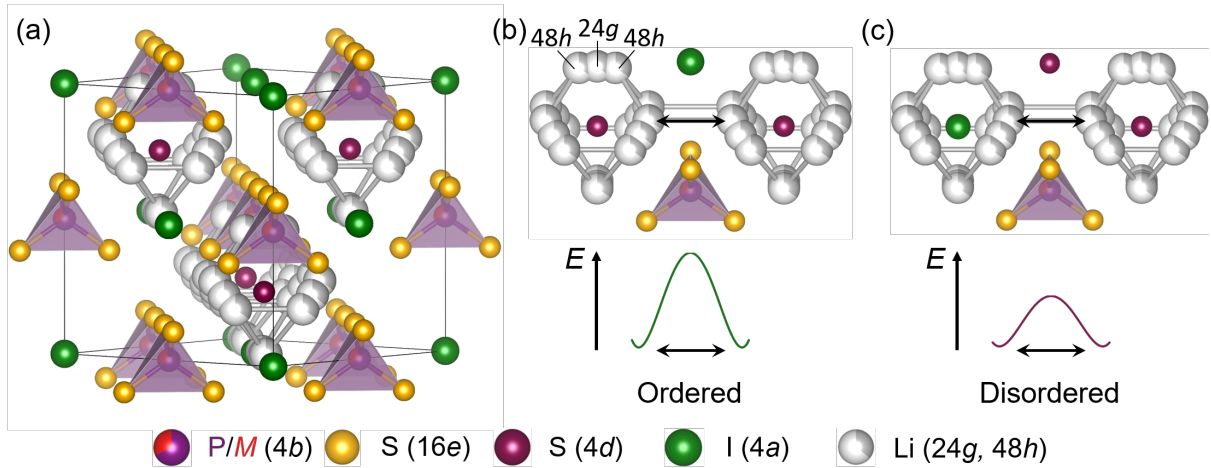
Figure 1: a) Crystal structure of $Li_6P_{1-x}M_xS_5I$ (M = Si, Ge, or Sn), in which the I^- form a face-centered cubic lattice, with PS_4^{3-} tetrahedra in the octahedral voids and free S^{2-} anions on half of the tetrahedral voids (Wyckoff 4d). The Li^+ forms pseudo-octahedral cages around the S^{2-} sites with two crystallographically distinct positions: Wyckoff 24g and 48h. b) For lithium-ion transport, the rate-determining step is the 48h – 48h inter-cage jump, which, in the fully ordered structure, requires lithium to move past a window involving the 4a iodine site and the sulfur of the PS_4 tetrahedra, as indicated by the arrows. c) A proposed mechanism of the energy land scape flattening, i.e. by either increasing the ground state energy or decreasing transition state (or both) in comparison to b). Introducing structural disorder flattens the potential energy landscape for long-range Li-ion migration.

2. Experimental Methods

Synthesis. Two series of elemental substitutions in the Li-argyrodites, $Li_{6+x}P_{1-x}M_xS_5I$, where M = Si or Sn, were prepared using a classic solid-state synthesis. Lithium sulfide (Li_2S, Alfa-Aesar, 99.9 %), lithium iodide (LiI, ultra-dry, 99.999 %, Alfa-Aesar), silicon powder (Si, ChemPUR, 99 %), tin powder (Sn, ChemPUR, 99.99 %), phosphorus pentasulfide (P_4S_{10}, Merck, 99 %), and sulfur (S_8, Acros Organics, 99.999 %), were used as precursors. The precursors in stoichiometric ratios were hand-ground in an agate mortar for 15 min, pelletized with a manual screw press and loaded into quartz ampoules. The quartz ampoules were carbon-coated and preheated at 800 °C under a dynamic vacuum to mitigate any parasitic reactions with the ampoule or residual water. The samples were sealed in the ampoules *in vacuo* (~ 10^{-3} mbar), followed by annealing at 550 °C for two weeks to complete the desired reaction. The resulting samples were hand-ground into a powder for the subsequent structure and transport characterizations. All preparations were carried out under an argon atmosphere. The exact

nominal compositions of samples prepared were as follows: $Li_{6+x}P_{1-x}Si_xS_5I$, where x_N = 0, 0.1, 0.2, 0.25, 0.3, 0.4, 0.5, 0.6, 0.7, and 0.8. $Li_{6+x}P_{1-x}Sn_xS_5I$, where x_N = 0.05, 0.1, 0.15, 0.2, 0.25, and 0.3.

X-ray powder diffraction. X-ray diffraction was carried out to obtain the lattice parameters and phase purities with a PANalytical Empyrean powder diffractometer in Bragg–Brentano geometry with Cu Kα radiation (λ_1 = 1.5406 Å, and λ_2 = 1.5444 Å). Measurements were carried out in the 2θ range between 10° and 90° with a step size of 0.026°. All powders were placed on (911)-oriented silicon zero background holders with a thin (7.5 μm) Kapton polyimide film to avoid exposure to air and moisture.

Neutron powder diffraction. To determine the Si content on the P site and to investigate the Li-substructure, high-resolution neutron powder diffraction data were collected on selected Si-substituted argyrodite samples $Li_{6+x}P_{1-x}Si_xS_5I$ with x = 0.25, 0.5, and 0.7. Measurements were performed in the Debye–Scherrer geometry at the Heinz Maier-Leibnitz Zentrum (research reactor FRM II, Garching b. München, Germany) on the high-resolution diffractometer SPODI.[47,48] Data collection was performed using a single wavelength, *i.e.*, monochromatic neutrons (λ = 1.54825(2) Å) that were obtained from the thermal neutron beam at a 155° takeoff angle using the 551 and 331 reflections of a vertically focused composite Ge monochromator of 200 mm height. The vertical-position-sensitive multidetector (300 mm vertical sensitivity range at 1.117 m sample-to-detector distance) consisting of 80 ^{3}He tubes and covering an angular range of 160° 2θ was used for data collection. The samples (approximately 2 cm^3 in volume) were filled into a thin-wall (0.15 mm) vanadium can (12 mm in diameter) under an argon atmosphere and then sealed using indium wire. The vanadium container was then mounted on a capillary spinner enabling sample rotation to minimize effects of preferred crystallite orientations. Two-dimensional powder diffraction data of the continuously rotated sample were collected and corrected for geometrical aberrations and detector nonlinearities.[49]

Rietveld analysis. Rietveld refinements were carried out using the TOPAS-Academic V6 software package.[50] A 2θ range of 10–26.5° was excluded from the refinements of the X-ray diffraction patterns in order to mitigate the interfering diffraction intensity from the polyimide film background.[15,31] The resultant structural data obtained with excluding the lower 2θ range are in good agreement with those from the neutron diffraction data over the whole measured 2θ range. The peak profile shape was described by a pseudo-Voigt function using the modified Thomson−Cox−Hastings setting. Fit indicators R_{wp} and the goodness-of-fit S were used to assess the quality of the refined structural models. The following parameters were initially

refined: (1) scale factor, (2) 10 and 20 coefficients for a Chebyshev polynomial background with X-ray and neutron, respectively, (3) peak shape, (4) lattice parameters including sample displacement, (5) fractional atomic coordinates, (6) isotropic atomic displacement parameters. Finally (7), atomic occupancies of the anions were then allowed to refine simultaneously with all other parameters, to quantify the anion site-disorder.

Electrochemical impedance spectroscopy. Total conductivities were measured by AC impedance spectroscopy, using pellets with vapor-deposited gold layers. The as-synthesized sample powder was pelletized by isostatic press under 325 MPa. Approximately 200 nm thick gold electrodes ($0.2 \ nm \ s^{-1}$) with the diameter of 8.2 mm were vapor deposited onto the pellets and the resulting pellets were sealed in pouch bags with Al contacts on the deposited gold layers for the transport measurements. Electrochemical impedance spectroscopy (EIS) was conducted using a VMP300 impedance analyzer (Bio-Logic Science Instruments) at frequencies from 7 MHz to 100 mHz with an amplitude of 10 mV in the temperature range of −40 to 60 °C (in climate chamber, Weiss Klimatechnik). The obtained spectra were first analyzed with Kramers-Kronig relations to determine the reliable frequency ranges for characterization. Finally, the conductivities were calculated through the resistances extracted by fitting impedance spectra using equivalent circuits. The high frequency range (> 1 MHz) was excluded from the fitting because of a larger uncertainty. All fits were performed using the RelaxIS software package (rhd Instruments, version 3). An error in the conductivity measurement is estimated to be 15 % and shown with the error bars.

3. Results & Discussion

Overall structural characterization. The lithium superionic argyrodites $Li_{6+x}P_{1-x}M_xS_5I$ with M = Si and Sn were synthesized with increasing M^{4+}/P^{5+} ratio in order to explore the structural changes and influences on the ionic transport properties. For the structural characterization, X-ray diffraction was initially employed. In addition, selected samples in $Li_{6+x}P_{1-x}Si_xS_5I$ were investigated using neutron diffraction due to the low X-ray scattering form factor for Li and the fact that Si^{4+} and P^{5+} are indistinguishable using X-ray diffraction. Figure 2 shows representative diffraction patterns for the X-ray and neutron scattering data of $Li_{6.5}P_{0.75}Si_{0.25}S_5I$, showing only minor impurities of LiI. In addition, for higher Si^{4+}/P^{5+} ratios, SiO_2 can also be identified in the neutron diffraction data. Comparisons of the obtained diffraction patterns are shown in Figure S1 – S3. All diffraction data were analyzed *via* Rietveld refinements and the

refined diffraction on all samples can be found tabulated in the Supporting Information (Tables S1 – S19).
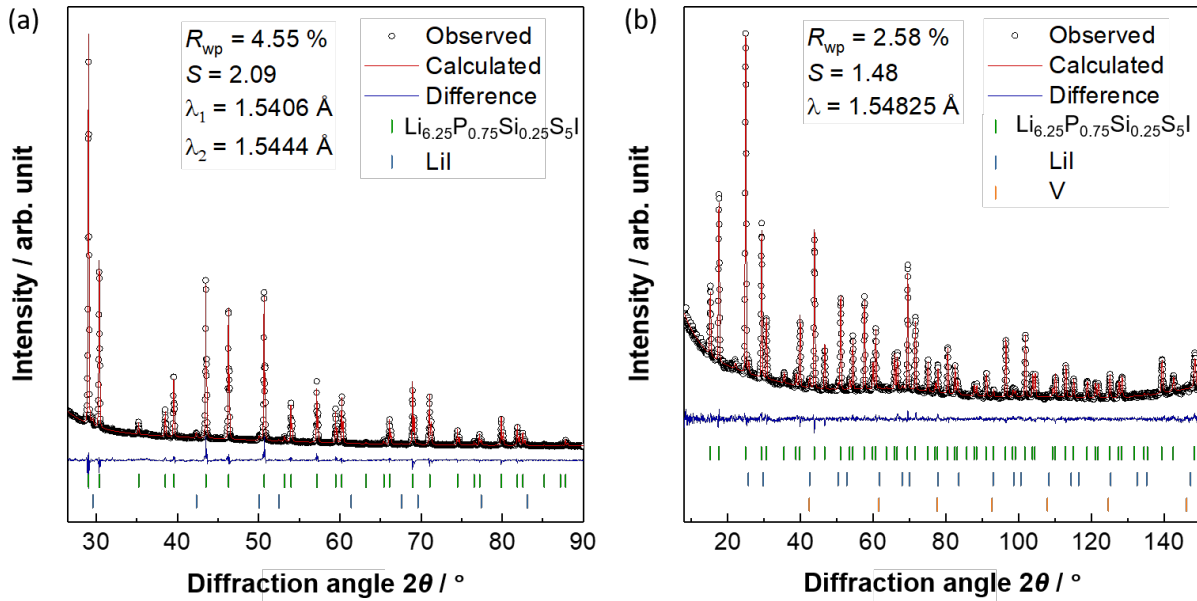

Figure 2: Representative (a) X-ray and (b) neutron diffraction patterns for Li$_{6.6}$P$_{0.75}$Si$_{0.25}$S$_5$I and the corresponding Rietveld refinements. Small fractions of impurity phases can be found that correspond to ~1.8 wt.% LiI in the X-ray diffraction data and ~2.6 wt.% LiI in the neutron diffraction data, along with reflections of the V sample holder. R$_{wp}$ and S are the weighted profile R-factor and the goodness of fit, respectively.

Recent aliovalent substitutions on the PS$_4^{3-}$ tetrahedra include the substitution of Si^{4+} in Li$_{6+x}$P$_{1-x}$Si$_x$S$_5$Br, showing a solubility limit around 30 at.% while the incorporation of Ge^{4+} in Li$_6$PS$_5$Br proved unsuccessful.[33] Further work showed the incorporation of Ge^{4+} in Li$_{6+x}$P$_{1-x}$Ge$_x$S$_5$I leading to an expansion of the unit cell, broadening of the lithium diffusion pathways and the onset of site-disorder between I$^-$ and S^{2-} for $x > 0.2$.[31] In order to compare the results of Si^{4+} and Sn^{4+} substitution with the changes found by Ge^{4+} incorporation, all of the obtained structural data are compared to the structural changes reported for Li$_{6+x}$P$_{1-x}$Ge$_x$S$_5$I.[31] Figure 3 shows the occurring structural changes during substitution in Li$_{6+x}$P$_{1-x}$M$_x$S$_5$I, with x_N indicating the nominal composition and x_R indicating the composition obtained from the occupancy refinements. With increasing nominal M^{4+}/P^{5+} ratio, an increase in the refined M^{4+} occupancy on the P^{5+} site and a monotonic increase in the lattice constant can be observed, indicating the successful formation of solid solutions (Figure 3a and b). The overall increase in the lattice parameters during the substitution is the largest for Sn and the smallest for Si, with

Ge in between, showing the differences in the ionic radii of $r(Sn^{4+}) = 0.55$ Å $> r(Ge^{4+}) = 0.39$ Å $> r(Si^{4+}) = 0.26$ Å $> r(P^{5+}) = 0.17$ Å for a tetrahedral coordination environment.[45] While a linear increase of the lattice parameter has been found in $Li_{6+x}P_{1-x}Ge_xS_5I$ up to $x = 0.8$, it remains constant afterwards indicating that a solubility limit has been reached. In contrast, for $Li_{6+x}P_{1-x}Sn_xS_5I$, a solubility limit can be found around 20 at.% Sn^{4+}, indicating that the larger Sn^{4+} exhibits a more limited solubility compared to Ge^{4+}. With further increasing Sn content, higher phase fractions of the impurity phases can be observed, *i.e.* LiI as well as reflections from undetermined phases, likely Li-Sn-S of nature. This behavior is consistent with the increased solubility of Si^{4+} in $Li_{6+x}P_{1-x}Si_xS_5Br$ compared to Ge^{4+}.[33] A slightly different behavior can be found for the metal occupancies in $Li_{6+x}P_{1-x}Si_xS_5I$. With increasing Si^{4+}/P^{5+} ratio, the lattice parameters increase linearly up to $x = 0.3$ with a subsequent minor deviation from linearity that corresponds with the onset of increasing impurity phases. However, despite the appearance of phase segregations, the lattice parameters further increase indicating that more Si^{4+} is incorporated into the structure and that a multiphase regime has been reached in the phase diagram. In order to corroborate the successful incorporation, the changes in the occupancy of M^{4+} on P^{5+} are shown in Figure 3b. While the substitution with Ge shows a much higher solubility of Ge^{4+} on the P^{5+} position, Sn^{4+} seems to exhibit a solubility limit below 20 at.%. The minor difference between the solubility limit determined from the lattice parameters and the refined occupancies is likely related to overlapping impurity reflections at higher ratios of Sn^{4+}/P^{5+}. Compared to Sn^{4+}, the neutron diffraction data show a solubility of Si^{4+} up to $x_N = 0.7$. However, the overall Si^{4+} content obtained from the refinement against the neutron diffraction data is lower than the nominal content, which is consistent with the decreasing slope in the lattice parameters. Accordingly, minor impurity reflections of SiO_2 can be found in samples with higher Si contents, which indicates the loss of Si as a stable oxide.

As not all compositions of $Li_{6+x}P_{1-x}Si_xS_5I$ were measured using neutron diffraction, a consistent comparison between the different compositions is challenging. While the values for $Li_{6+x}P_{1-x}Ge_xS_5I$ and $Li_{6+x}P_{1-x}Sn_xS_5I$ are shown against the extracted compositions from the Rietveld refinements (Figure 3b), x_R cannot be fully resolved in the $Li_{6+x}P_{1-x}Si_xS_5I$ series of solid solutions due to the fact that Si^{4+} and P^{5+} are indistinguishable in X-ray diffraction. In order to be able to make a fair comparison, the refined occupancies of the Si^{4+} on the P^{5+} position against the neutron diffraction data (Figure 3b) were used to obtain a *calibration curve* (Figure S4). Here, the linearity in the occupancy is used to calculate a refined x_R in relation to the nominal composition and lattice parameters (See Supporting Information for details). While

this approach will likely lead to deviations from the true occupancies, usage of the nominal composition does not seem appropriate considering the lower refined occupancy of Si^{4+} relative to the nominal values.
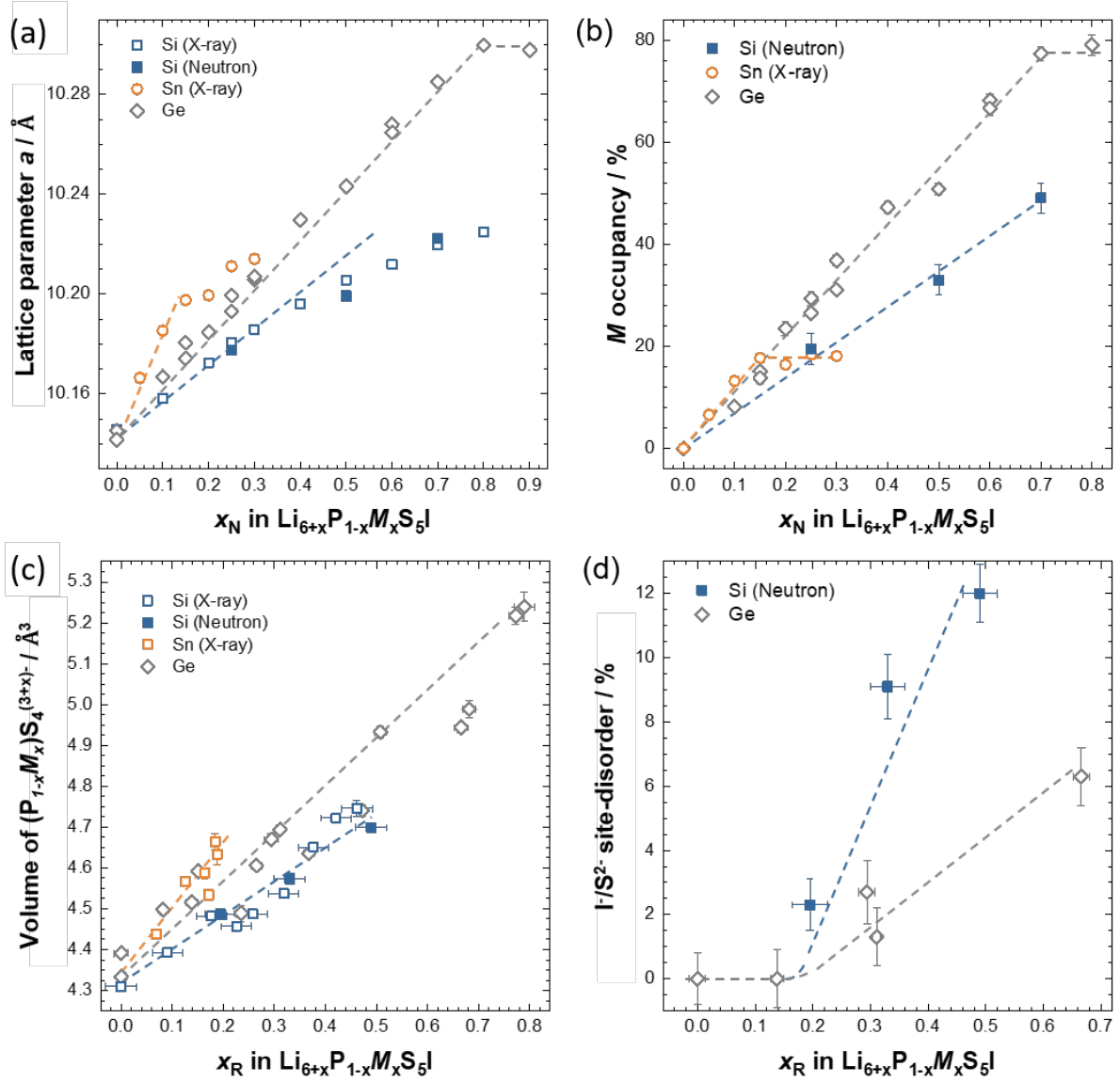

Figure 3: a) Lattice parameters of the solid solutions $Li_{6+x}P_{1-x}M_xS_5I$ vs. nominal M content x_N. With increasing M^{4+} content, the unit cell expands until a solubility limit is reached that corresponds to the maximum solubility of ~ 80 % Ge^{4+} on the P^{5+} position, while a plateau appears with Sn^{4+} at around 20 % as shown in b). As for the Si^{4+} substitution, a monotonic increase in the lattice constant and the refined occupancy can be seen, however there is a slight deviation from the ideal substitution content, indicating that the sample compositions exhibit multi-phase equilibria. c) Increasing $(M^{4+}/P^{5+})S_4^{(3+x)-}$ tetrahedral volume during the substitution of the larger M^{4+} for P^{5+} against the refined M occupancy x_R. d) While the unsubstituted I-argyrodite is known to exhibit a fully ordered structure,[32] the substitution with

9

M leads to a growing S^{2-}/I^- site-disorder starting around 20 at.% of M^{4+}. All the structural data of Ge-substitution series are taken from Kraft et al.[31]

Figure 3c shows the changing polyhedral volumes of $(P_{1-x}M_x)S_4^{(3+x)-}$ against the refined metal contents x_R. With increasing M^{4+} occupancy, the polyhedra expand, confirming the successful incorporation of M^{4+} on the P^{5+} site. While there is some degree of scatter in the data for $Li_{6+x}P_{1-x}Ge_xS_5I$, it can be seen that the changes within the polyhedral volumes correlate well with the ionic radii of $r(Sn^{4+}) > r(Ge^{4+}) > r(Si^{4+})$. Furthermore, similar to the recently shown onset of site-disorder between I^- and S^{2-} in $Li_{6+x}P_{1-x}Ge_xS_5I$ at $x > 0.2$, the incorporation of Si^{4+} induces this site-disorder as well (Figure 3d). While no site-disorder can be found in $Li_{6+x}P_{1-x}Sn_xS_5I$, due to the limited solubility of Sn^{4+} in the structure, the Si^{4+} substitution actually leads to slightly larger values for the site-disorder relative to Ge^{4+}, though the onset of the site-disorder in both systems occurs around $0.2 \leq x \leq 0.25$, suggesting that a similar mechanism triggers this disorder.

Lithium substructure. In addition to the structural changes of the $(P_{1-x}M_x)S_4^{(3+x)-}$ tetrahedra and the occurring I^-/S^{2-} site-disorder, the neutron diffraction data enables an investigation of the changes in the Li^+ substructure (Figure 4). Here, only the neutron diffraction data for $Li_{6+x}P_{1-x}Si_xS_5I$ are compared to $Li_{6+x}P_{1-x}Ge_xS_5I$, as the solubility limit in $Li_{6+x}P_{1-x}Sn_xS_5I$ is too low to observe the sharp reduction in the activation energy (See Ionic Transport section). With increasing M^{4+} occupancy, the Li^+ occupancy on the $24g$ site increases (Figure 4a) and essentially all additional Li^+ occupies this site. As previously observed,[31,33] the increasing Li^+ occupancy on the $24g$ site leads to larger Coulombic repulsion, which results in the longer doublet distance $48h - 24g - 48h$. In addition, a minor decrease of the distance between the Li^+ cages (i.e. the *inter*-cage distance) can be found. Furthermore, for both substituents, the tetrahedral volume of the $Li(48h)S_3I$ polyhedra and the area of the $Li(24g)S_3$ triangular plane increase. Here, the $Li(48h)S_3I$ polyhedra represent the bottleneck for the long-range *inter*-cage jump and the wider diffusion pathways for Li^+ in the structure have been linked to a higher mobility of the cations.[39]

Despite the clear influence of the larger unit cell and increasing Li^+ content on the lithium substructure itself, no significant differences can be found between the $Li_{6+x}P_{1-x}Si_xS_5I$ and $Li_{6+x}P_{1-x}Ge_xS_5I$ systems. The lithium occupancies on $48h$ and $24g$, as well as the lithium jump distances and width of the diffusion pathways seem to be independent of the cation size of M^{4+},

but rather dependent on the lithium occupancy alone. It is remarkable that a larger unit cell volume in $Li_{6+x}P_{1−x}Ge_xS_5I$ does not lead to significant changes in the width of the diffusion pathways, as compared to the smaller lattice in $Li_{6+x}P_{1−x}Si_xS_5I$. These data indicate that the overall change in the lattice volume may not be as influential on the lithium substructure in ionic conductors as the number of lithium cations per unit cell.
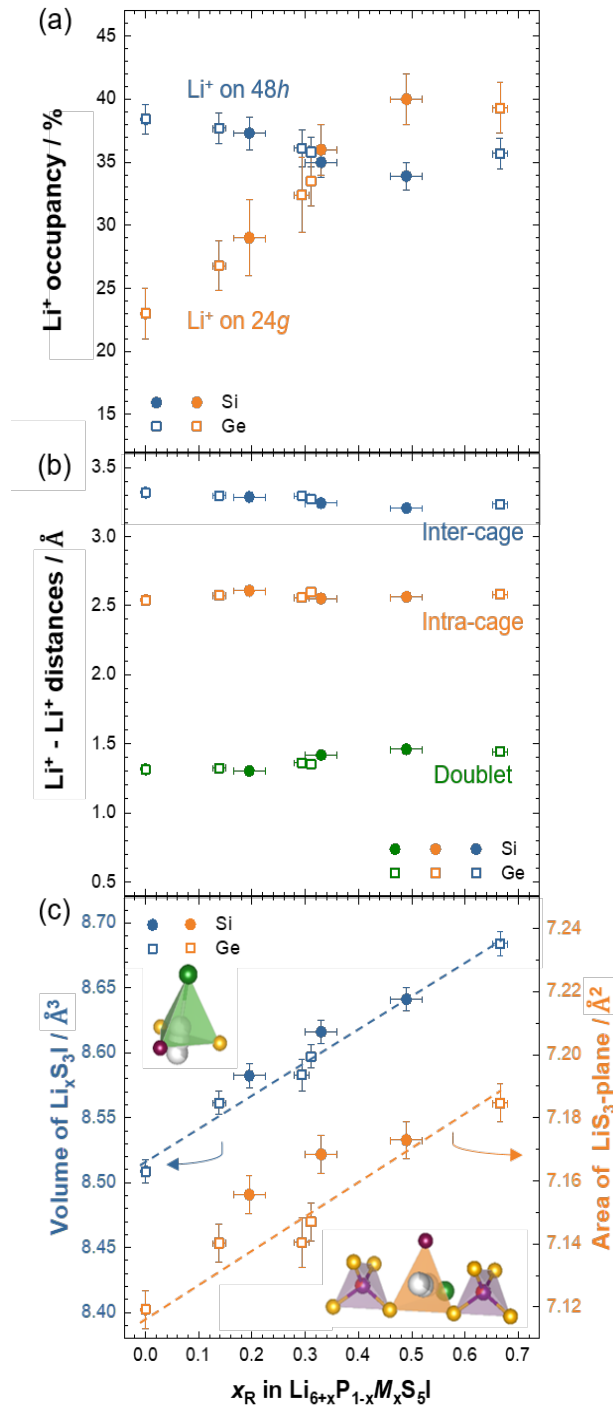
Figure 4: Changes to the Li-substructure in $Li_{6+x}P_{1-x}Si_xS_5I$ compared to $Li_{6+x}P_{1-x}Ge_xS_5I$, as obtained from the neutron diffraction data as a function of the refined Si or Ge content x_R. All filled symbols are data from Si-substitutions and open symbols are from Ge-substitutions reported by Kraft et al.[31] With increasing M^{4+} occupancy, additional Li^+ is incorporated into the structure. a) Percentage of sites occupied by Li^+ with the additional Li^+ being placed on the Wyckoff 24g position. b) The increasing Li^+ concentration induces an increase in the distance between the 48h − 24g − 48h positions (doublet distance) and a decreasing jump distance between the Li^+ cages (inter-cage jump). c) With increasing unit cell size and size of the adjacent $(P_{1-x}M_x)S_4^{(3+x)-}$ tetrahedra, the $Li(48h)S_3I$ polyhedra and $Li(24g)S_3$ triangle areas expand, corresponding to wider diffusion pathways for Li^+.

Ionic transport. Temperature-dependent impedance spectroscopy was performed to assess the changes to the ionic conductivity upon addition of Si^{4+} and Sn^{4+} on $Li_{6+x}P_{1-x}M_xS_5I$ for comparison with the $Li_{6+x}P_{1-x}Ge_xS_5I$ series. Representative impedance responses for $Li_{6.5}P_{0.5}Si_{0.5}S_5I$ and $Li_{6.2}P_{0.8}Sn_{0.2}S_5I$, as well as the Arrhenius plots of all samples, can be found in Figure 5. For comparison, all impedance spectra obtained at room temperature for all compositions can be found in the Supporting Information (Figure S5). All impedance spectra were initially fit with an equivalent circuit consisting of one parallel constant phase element (CPE)/resistor in series with a CPE, representing the Au electrodes. A series circuit of a resistor and a CPE was employed as necessary for spectra from the highly conductive samples, as seen in Figure 5a for the measurements at temperatures above room temperature. This is because, in the samples with a higher degree of substitution, only the tail of the blocking electrodes can be used for the fit. The resolvable impedance spectra exhibit α-values of > 0.8, representing the ideality of the CPE,[51] and capacitances between 24 and 110 pF. All conductivities and capacitances obtained by the impedance are tabulated in the Supporting Information (Tables S20 − S21). Bulk and grain boundary contributions cannot be de-convoluted, however, the obtained ideality of the semi-circle and capacitances correspond well with bulk transport,[52] as typically observed for these Li^+ conducting argyrodites.[32,33]
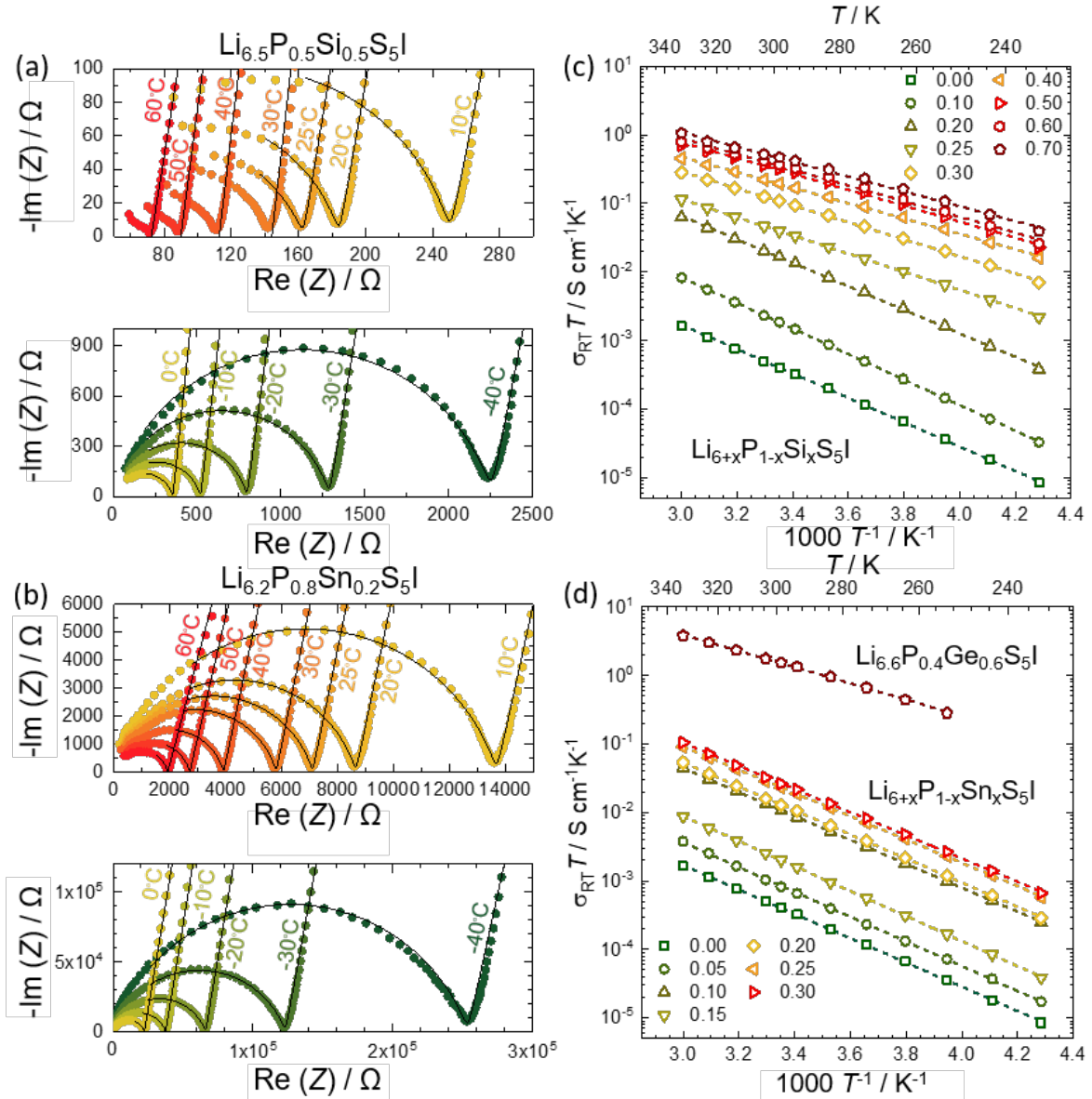
Figure 5: a) and b) Nyquist plots of the representative solid solutions measured between −40 °C and 60 °C. c) and d) Arrhenius plots of the conductivity values for $Li_{6+x}P_{1-x}M_xS_5I$ (M = Si, Sn), as well as the representative data of Ge substitution in d), taken from Kraft et al.[31] All listed compositions are nominal. The conductivity of both Si- and Ge-substitutions decrease at $x_N > 0.8$ due to the appearance of side phases.

Figure 6a shows the obtained conductivities of $Li_{6+x}P_{1-x}M_xS_5I$ (M = Si, Sn) at room temperature and the comparison to the literature values of $Li_{6+x}P_{1-x}Ge_xS_5I$.[31] In addition, Figure 6b shows the activation barriers for Li^+ migration as extracted from the Arrhenius plots. Using the extracted x_R in $Li_{6+x}P_{1-x}M_xS_5I$ (M = Si, Sn) shows an increasing ionic conductivity over several orders of magnitude for M = Si, similar to $Li_{6+x}P_{1-x}Ge_xS_5I$.[31] Whereas the substitution with Sn^{4+} only increases the conductivity up to $\sigma = 0.1 \pm 0.015$ mS cm^{-1} due to the limited solubility, a

maximum conductivity of $\sigma = 2.0 \pm 0.3$ mS cm^{-1} can be found for the nominal composition of Li$_{6.7}$P$_{0.3}$Si$_{0.7}$S$_5$I (with x_R = 0.46). For comparison, a maximum conductivity of $\sigma = 5.4 \pm 0.8$ mS cm^{-1} was found for Li$_{6.6}$P$_{0.4}$Ge$_{0.6}$S$_5$I.[31] Here, the differences in the solubility limits and the phase purity between Si and Ge on the P site likely leads to different compositions x_R exhibiting the highest conductivity. Similar to Li$_{6+x}$P$_{1-x}$Ge$_x$S$_5$I,[31] the observed changes in the conductivity cannot be directly explained by the minor increase in the lithium content and the activation barrier clearly has a significant influence on the transport (see Figure 6b). With increasing x_R, the activation barrier initially remains constant before undergoing a significant drop with an inflection point around $x_R = 0.25$, as recently observed for Li$_{6+x}$P$_{1-x}$Ge$_x$S$_5$I.[31]
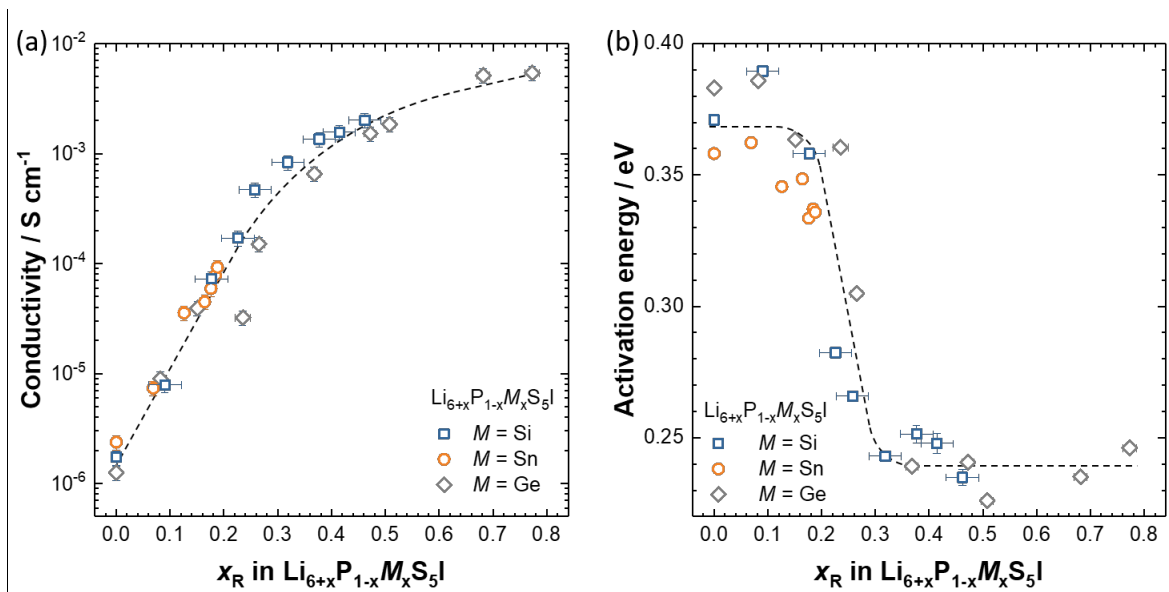
Figure 6: Ionic conductivity (a) and activation barrier (b) of Li$_{6+x}$P$_{1-x}$M$_x$S$_5$I as a function of the refined M content. With increasing M^{4+} and Li$^+$ concentration, the ionic conductivity increases over three orders of magnitude and exhibits an inflection point starting ~ 20 – 25 % of M that leads to a strong decrease of the activation barrier. Data of Ge-substitution series are obtained from Kraft et al.[31]

Discussion. The data and trends found in the solid solutions of Li$_{6+x}$P$_{1-x}$M$_x$S$_5$I (M = Si, Sn) show that similar to Li$_{6+x}$P$_{1-x}$Ge$_x$S$_5$I the substitutions can have a tremendous influence on the ionic transport in the argyrodite structure. While the limited solubility of Sn does not allow for major changes to the structure and the activation energy, the incorporation of Si^{4+} into Li$_{6+x}$P$_{1-x}$M$_x$S$_5$I and the comparison with Li$_{6+x}$P$_{1-x}$Ge$_x$S$_5$I allows for the following observations:

1) The larger ionic radius of Sn^{4+} does not allow for full incorporation into the structure, whereas large fractions of Si^{4+} and Ge^{4+} can be incorporated. Despite the different solubility limits, the trend in the ionic radii of $r(Sn^{4+}) > r(Ge^{4+}) > r(Si^{4+})$ determines the change in the unit cell parameters, as well as the tetrahedral volumes of $(P_{1-x}M_x)S_4^{(3+x)-}$.

2) The Rietveld refinements show an increase in the I^-/S^{2-} site-disorder for Si at a value of $x_R = 0.25$. This site-disorder has recently been suggested to lead to an energy landscape flattening in $Li_{6+x}P_{1-x}Ge_xS_5I$ in which the occurrence of disorder leads to a sharp decrease of the activation barrier. Whereas it is unclear if the effect lowers the transition state energy or increases the energy of initial state (or both),it is believed that the disorder opens up low-energy inter-cage jump pathways and percolation becomes possible, whereas a local ordering of I^- and S^{2-} are detrimental for the long-range ionic jumps. While the Sn substitution cannot lead to high enough unit cell volumes and lithium contents, the onset of the drop in the activation barrier in $Li_{6+x}P_{1-x}Si_xS_5I$ coincides with the onset of site-disorder as it was observed in $Li_{6+x}P_{1-x}Ge_xS_5I$. This suggests that indeed, the flattening of the energy landscape is directly correlated with a local ordering and that structural changes can have a tremendous influence on the ionic transport in argyrodites. Tailoring of the structural disorder clearly enables the enhancement of the ionic conductivity of solid electrolytes.

3) The final observation is that within $Li_{6+x}P_{1-x}Si_xS_5I$ and $Li_{6+x}P_{1-x}Ge_xS_5I$, the lithium substructure seems to be mostly influenced by the increasing lithium content and not the overall changes to the structural framework. While the differences in the ionic radii between Si^{4+} and Ge^{4+} lead to different polyhedral volumes of the $(P_{1-x}M_x)S_4^{(3+x)-}$ tetrahedra and differences in the unit cell volume, the observed $Li^+ - Li^+$ distances, the Li^+ occupancies and the observed width of the lithium diffusion pathways ($Li(48h)S_3I$ polyhedral volume and area of the $Li(24g)S_3$ triangular plane) exhibit similar values and trends along both series of solid solutions. In contrast to the common belief that the substituents themselves will affect the lithium substructures and diffusion pathways, the lithium content and $Li^+ - Li^+$ interactions are likely having a much stronger influence in the $Li_{6+x}P_{1-x}M_xS_5I$ series.

5. Conclusion

In this work, aliovalent substitutions in $Li_{6+x}P_{1-x}M_xS_5I$, with M = Si and Sn, were performed and their structural and transport properties were compared with the previously reported $Li_{6+x}P_{1-x}Ge_xS_5I$. Using a combination of X-ray and neutron diffraction, the evolution of the unit cell volume, M^{4+}/P^{5+} ratios, solubility limits of Si^{4+} and Sn^{4+}, changes in the Li^+ substructures and the onset of I^-/S^{2-} site-disorder could be resolved. Impedance spectroscopy revealed that there is a sharp reduction in the activation energy in $Li_{6+x}P_{1-x}Si_xS_5I$ at the same M^{4+}/P^{5+} composition as previously found in the Ge-analogue, suggesting a general mechanism behind the ionic conductivity enhancement and the observed flattening of the energy landscape. In contrast, no significant variation in the energy landscape could be found in the $Li_{6+x}P_{1-x}Sn_xS_5I$ series due to the limited solubility of Sn. Notably, the successful substitutions enhanced the Li-ion conductivities significantly, resulting in a room-temperature ionic conductivity of 2.0 ± 0.3 mS cm^{-1} for $Li_{6.7}P_{0.3}Si_{0.7}S_5I$ and 0.1 ± 0.015 mS cm^{-1} for $Li_{6.3}P_{0.7}Sn_{0.3}S_5I$, whereas the unsubstituted Li_6PS_5I exhibits only 10^{-3} mS cm^{-1}. Lastly, despite the significantly different ionic radii of the substituents, almost identical Li^+ substructures with the same M^{4+}/P^{5+} ratio were observed upon Si- and Ge-substitutions, which indicates a greater influence of the Li^+ content on the Li^+ substructure over the noted changes to the lattice.

These observations highlight the importance of a detailed structural analysis and future molecular dynamics simulations in order to understand the underlying mechanism of the energy landscape flattening observed in $Li_{6+x}P_{1-x}M_xS_5I$. Gaining a better understanding of the structure-property relationships at play in ionic conductors paves the way for further enhancements to the ionic conductivities in solid electrolytes and, consequently, the improvement of all-solid-state batteries.

Supporting Information

Neutron and X-ray patterns of both $Li_{6+x}P_{1-x}Si_xS_5I$ and $Li_{6+x}P_{1-x}Sn_xS_5I$ series, a description of the estimation of Si contents with X-ray data based on neutron refinement, all refined data obtained by refining X-ray and neutron data, the comparison of impedance spectra of all samples measured at 25 °C, and the parameters used for fitting the impedance spectra at various temperature.

AUTHOR INFORMATION

Corresponding Authors

*wolfgang.g.zeier@pc.jlug.de;

Notes

The authors declare no competing financial interests.

References

(1)   Janek, J.; Zeier, W. G. A Solid Future for Battery Development. *Nat. Energy* **2016**, *1*, 16141.

(2)   Koerver, R.; Zhang, W.; de Biasi, L.; Schweidler, S.; Kondrakov, A.; Kolling, S.; Brezesinski, T.; Hartmann, P.; Zeier, W.; Janek, J. Chemo-Mechanical Expansion of Lithium Electrode Materials – On the Route to Mechanically Optimized All-Solid-State Batteries. *Energy Environ. Sci.* **2018**, *11*, 2142–2158.

(3)   Zhang, W.; Schröder, D.; Arlt, T.; Manke, I.; Koerver, R.; Pinedo, R.; Weber, D. A.; Sann, J.; Zeier, W. G.; Janek, J. (Electro)Chemical Expansion during Cycling: Monitoring the Pressure Changes in Operating Solid-State Lithium Batteries. *J. Mater. Chem. A* **2017**, *5*, 9929–9936.

(4)   Zhang, W.; Leichtweiß, T.; Culver, S. P.; Koerver, R.; Das, D.; Weber, D. A.; Zeier, W. G.; Janek, J. The Detrimental Effects of Carbon Additives in $Li_{10}GeP_2S_{12}$-Based Solid-State Batteries. *ACS Appl. Mater. Int.* **2017**, *9*, 35888–35896.

(5)   Koerver, R.; Aygün, I.; Leichtweiß, T.; Dietrich, C.; Zhang, W.; Binder, J. O.; Hartmann, P.; Zeier, W. G.; Janek, J. Capacity Fade in Solid-State Batteries: Interphase Formation and Chemomechanical Processes in Nickel-Rich Layered Oxide Cathodes and Lithium Thiophosphate Solid Electrolytes. *Chem. Mater.* **2017**, *29*, 5574–5582.

(6)   Koerver, R.; Walther, F.; Aygün, I.; Sann, J.; Dietrich, C.; Zeier, W. G.; Janek, J. Redox-

Active Cathode Interphases in Solid-State Batteries. *J. Mater. Chem. A* **2017**, *5*, 22750–22760.

(7)   Auvergniot, J.; Cassel, A.; Ledeuil, J. B.; Viallet, V.; Seznec, V.; Dedryvère, R. Interface Stability of Argyrodite Li_6PS_5Cl toward $LiCoO_2$, $LiNi_{1/3}Co_{1/3}Mn_{1/3}O_2$, and $LiMn_2O_4$ in Bulk All-Solid-State Batteries. *Chem. Mater.* **2017**, *29*, 3883–3890.

(8)   Auvergniot, J.; Cassel, A.; Foix, D.; Viallet, V.; Seznec, V.; Dedryvère, R. Redox Activity of Argyrodite Li_6PS_5Cl Electrolyte in All-Solid-State Li-Ion Battery: An XPS Study. *Solid State Ionics* **2017**, *300*, 78–85.

(9)   Richards, W. D.; Miara, L. J.; Wang, Y.; Kim, J. C.; Ceder, G. Interface Stability in Solid-State Batteries. *Chem. Mater.* **2016**, *28*, 266–273.

(10)   Hakari, T.; Deguchi, M.; Mitsuhara, K.; Ohta, T.; Saito, K.; Orikasa, Y.; Uchimoto, Y.; Kowada, Y.; Hayashi, A.; Tatsumisago, M. Structural and Electronic-State Changes of a Sulfide Solid Electrolyte during the Li Deinsertion-Insertion Processes. *Chem. Mater.* **2017**, *29*, 4768–4774.

(11)   Ohno, S.; Koerver, R.; Dewald, G.; Rosenbach, C.; Titscher, P.; Steckermeier, D.; Kwade, A.; Janek, J.; Zeier, W. G. Observation of Chemomechanical Failure and the Influence of Cutoff Potentials in All-Solid-State Li–S Batteries. *Chem. Mater.* **2019**, *31*, 2930-2940.

(12)   Walther, F.; Koerver, R.; Fuchs, T.; Ohno, S.; Sann, J.; Rohnke, M.; Zeier, W. G.; Janek, J. Visualization of the Interfacial Decomposition of Composite Cathodes in Argyrodite Based All-Solid-State Batteries Using Time-of-Flight Secondary Ion Mass Spectrometry. *Chem. Mater.* **2019**, acs.chemmater.9b00770.

(13)   Ganapathy, S.; Yu, C.; van Eck, E. R. H.; Wagemaker, M. Peeking across Grain Boundaries in a Solid-State Ionic Conductor. *ACS Energy Lett.* **2019**, 4, 1092–1097.

(14)   Kato, Y.; Hori, S.; Saito, T.; Suzuki, K.; Hirayama, M.; Mitsui, A.; Yonemura, M.; Iba, H.; Kanno, R. High-Power All-Solid-State Batteries Using Sulfide Superionic Conductors. *Nat. Energy* **2016**, *1*, 16030.

(15)   Krauskopf, T.; Culver, S. P.; Zeier, W. G. Bottleneck of Diffusion and Inductive Effects in $Li_{10}Ge_{1-x}Sn_xP_2S_{12}$. *Chem. Mater.* **2018**, *30*, 1791–1798.

(16)   Weber, D. A.; Senyshyn, A.; Weldert, K. S.; Wenzel, S.; Zhang, W.; Kaiser, R.; Berendts, S.; Janek, J.; Zeier, W. G. Structural Insights and 3D Diffusion Pathways within the Lithium Superionic Conductor $Li_{10}GeP_2S_{12}$. *Chem. Mater.* **2016**, *28*, 5905–5915.

(17) Kwon, O.; Hirayama, M.; Suzuki, K.; Kato, Y.; Saito, T.; Yonemura, M.; Kamiyama, T.; Kanno, R. Synthesis, Structure, and Conduction Mechanism of the Lithium Superionic Conductor $Li_{10+\delta}Ge_{1+\delta}P_{2-\delta}S_{12}$. *J. Mater. Chem. A* **2015**, *3*, 438–446.

(18) Kato, Y.; Saito, R.; Sakano, M.; Mitsui, A.; Hirayama, M.; Kanno, R. Synthesis, Structure and Lithium Ionic Conductivity of Solid Solutions of $Li_{10}(Ge_{1-x}M_x)P_2S_{12}$ (M = Si, Sn). *J. Pow. Source* **2014**, *271*, 60–64.

(19) Kamaya, N.; Homma, K.; Yamakawa, Y.; Hirayama, M.; Kanno, R.; Yonemura, M.; Kamiyama, T.; Kato, Y.; Hama, S.; Kawamoto, K.; et al. A Lithium Superionic Conductor. *Nat. Mater.* **2011**, *10*, 682–686.

(20) Kuhn, A.; Koehler, J.; Lotsch, B. V. Single-Crystal X - Ray Structure Analysis of the Superionic Conductor $Li_{10}GeP_2S_{12}$. *Phys. Chem. Chem. Phys.* **2013**, *15*, 11620–11622.

(21) Kuhn, A.; Duppel, V.; Lotsch, B. V. Tetragonal $Li_{10}GeP_2S_{12}$ and Li_7GePS_8-Exploring the Li Ion Dynamics in LGPS Li Electrolytes. *Energy Environ. Sci.* **2013**, *6*, 3548–3552.

(22) Kuhn, A.; Gerbig, O.; Zhu, C.; Falkenberg, F.; Maier, J.; Lotsch, B. V. A New Ultrafast Superionic Li-Conductor: Ion Dynamics in $Li_{11}Si_2PS_{12}$ and Comparison with Other Tetragonal LGPS-Type Electrolytes. *Phys. Chem. Chem. Phys.* **2014**, *16*, 14669–14674.

(23) Leube, B. T.; Inglis, K. K.; Carrington, E. J.; Sharp, P. M.; Shin, J. F.; Neale, A. R.; Manning, T. D.; Pitcher, M. J.; Hardwick, L. J.; Dyer, M. S.; et al. Lithium Transport in $Li_{4.4}M_{0.4}M'_{0.6}S_4$ (M = Al^{3+}, Ga^{3+}, and M' = Ge^{4+}, Sn^{4+}): Combined Crystallographic, Conductivity, Solid State NMR, and Computational Studies. *Chem. Mater.* **2018**, *30*, 7183–7200.

(24) Murayama, M.; Kanno, R.; Irie, M.; Ito, S.; Hata, T.; Sonoyama, N.; Kawamoto, Y. Synthesis of New Lithium Ionic Conductor Thio-LISICON—Lithium Silicon Sulfides System. *J. Solid State Chem.* **2002**, *168*, 140–148.

(25) Stöffler, H.; Zinkevich, T.; Yavuz, M.; Senyshyn, A.; Kulisch, J.; Hartmann, P.; Adermann, T.; Randau, S.; Richter, F. H.; Janek, J.; et al. Li^+-Ion Dynamics in β-Li_3PS_4 Observed by NMR: Local Hopping and Long-Range Transport. *J. Phys. Chem. C* **2018**, *122*, 15954–15965.

(26) Seino, Y.; Nakagawa, M.; Senga, M.; Higuchi, H.; Takada, K.; Sasaki, T. Analysis of the Structure and Degree of Crystallisation of $70Li_2S–30P_2S_5$ Glass Ceramic. *J. Mater. Chem. A* **2015**, *3*, 2756–2761.

(27) Seino, Y.; Ota, T.; Takada, K.; Hayashi, A.; Tatsumisago, M. A Sulphide Lithium Super Ion Conductor Is Superior to Liquid Ion Conductors for Use in Rechargeable Batteries.

Energy Environ. Sci. **2014**, *7*, 627–631.

(28)   Dietrich, C.; Weber, D.; Sedlmaier, S. J.; Indris, S.; Culver, S.; Walter, D.; Janek, J.; Zeier, W. Lithium Ion Conductivity in Li_2S-P_2S_5 Glasses – Building Units and Local Structure Evolution during the Crystallization of the Superionic Conductors Li_3PS_4, $Li_7P_3S_{11}$ and $Li_4P_2S_7$. *J. Mater. Chem. A* **2017**.

(29)   Ohtomo, T.; Hayashi, A.; Tatsumisago, M.; Kawamoto, K. Characteristics of the Li_2O–Li_2S–P_2S_5 Glasses Synthesized by the Two-Step Mechanical Milling. *J. Non. Cryst. Solids* **2013**, *364*, 57–61.

(30)   De Klerk, N. J. J.; Rosłoń, I.; Wagemaker, M. Diffusion Mechanism of Li Argyrodite Solid Electrolytes for Li-Ion Batteries and Prediction of Optimized Halogen Doping: The Effect of Li Vacancies, Halogens, and Halogen Disorder. *Chem. Mater.* **2016**, *28*, 7955–7963.

(31)   Kraft, M. A.; Ohno, S.; Zinkevich, T.; Koerver, R.; Culver, S. P.; Senyshyn, A.; Indris, S.; Morgan, B. J.; Zeier, W. G. Inducing High Ionic Conductivity in the Lithium Superionic Argyrodites $Li_{6+x}P_{1-x}Ge_xS_5I$ for All-Solid-State Batteries. *J. Am. Chem. Soc.* **2018**, *140*, 16330–16339.

(32)   Kraft, M. A.; Culver, S. P.; Calderon, M.; Böcher, F.; Krauskopf, T.; Senyshyn, A.; Dietrich, C.; Zevalkink, A.; Janek, J.; Zeier, W. G. Influence of Lattice Polarizability on the Ionic Conductivity in the Lithium Superionic Argyrodites Li_6PS_5X (X = Cl, Br, I). *J. Am. Chem. Soc.* **2017**, *139*, 10909–10918.

(33)   Minafra, N.; Culver, S. P.; Krauskopf, T.; Senyshyn, A.; Zeier, W. G. Effect of Si Substitution on the Structural and Transport Properties of Superionic Li-Argyrodites. *J. Mater. Chem. A* **2018**, *6*, 645–651.

(34)   Deiseroth, H. J.; Kong, S. T.; Eckert, H.; Vannahme, J.; Reiner, C.; Zaiß, T.; Schlosser, M. Li_6PS_5X: A Class of Crystalline Li-Rich Solids with an Unusually High Li^+ Mobility. *Angew. Chem. Int. Ed.* **2008**, *47*, 755–758.

(35)   Zhou, L.; Park, K.-H.; Sun, X.; Lalère, F.; Adermann, T.; Hartmann, P.; Nazar, L. F. Solvent-Engineered Design of Argyrodite Li_6PS_5X (X = Cl, Br, I) Solid Electrolytes with High Ionic Conductivity. *ACS Energy Lett.* **2019**, *4*, 265–270.

(36)   Yu, C.; Hageman, J.; Ganapathy, S.; van Eijck, L.; Zhang, L.; Adair, K. R.; Sun, X.; Wagemaker, M. Tailoring Li_6PS_5Br Ionic Conductivity and Understanding of Its Role in Cathode Mixtures for High Performance All-Solid-State Li–S Batteries. *J. Mater. Chem. A* **2019**, *7*, 10412–10421.

(37)   Adeli, P.; Bazak, J. D.; Park, K.-H.; Kochetkov, I.; Huq, A.; Goward, G.; Nazar, L. Boosting Solid-State Diffusivity and Conductivity in Lithium Superionic Argyrodites by Halide Substitution. *Angew. Chemie Int. Ed*. **2019**. DOI: 10.1002/anie.201814222

(38)   Krauskopf, T.; Muy, S.; Culver, S. P.; Ohno, S.; Delaire, O.; Shao-Horn, Y.; Zeier, W. G. Comparing the Descriptors for Investigating the Influence of Lattice Dynamics on Ionic Transport Using the Superionic Conductor $Na_3PS_{4-x}Se_x$. *J. Am. Chem. Soc.* **2018**, *140*, 14464–14473.

(39)   Culver, S. P.; Krauskopf, T.; Koerver, R.; Zeier, W. G. Designing Ionic Conductors: The Interplay between Structural Phenomena and Interfaces in Thiophosphatebased Solid-State Batteries. *Chem. Mater.* **2018**, *30*, 4179–4192.

(40)   Muy, S.; Bachman, J. C.; Giordano, L.; Chang, H.-H.; Abernathy, D. L.; Bansal, D.; Delaire, O.; Hori, S.; Kanno, R.; Maglia, F.; et al. Tuning Mobility and Stability of Lithium Ion Conductors Based on Lattice Dynamics. *Energy Environ. Sci.* **2018**, *11*, 850–859.

(41)   Krauskopf, T.; Culver, S. P.; Zeier, W. G. Local Tetragonal Structure of the Cubic Superionic Conductor Na_3PS_4. *Inorg. Chem.* **2018**, *57*, 4739–4744.

(42)   Breuer, S.; Pregartner, V.; Lunghammer, S.; Wilkening, M. Dispersed Solid Conductors: Fast Interfacial Li-Ion Dynamics in Nanostructured LiF and LiF: γ -Al 2 O 3 Composites. *J. Phys. Chem C* **2019**, DOI: 10.1021/acs.jpcc.8b10978.

(43)   Adelstein, N.; Wood, B. C. Role of Dynamically Frustrated Bond Disorder in a Li^+ Superionic Solid Electrolyte. *Chem. Mater.* **2016**, *28*, 7218–7231.

(44)   Bernges, T.; Culver, S. P.; Minafra, N.; Koerver, R.; Zeier, W. G. Competing Structural Influences in the Li Superionic Conducting Argyrodites $Li_6PS_{5-x}Se_xBr$ ($0 \leq x \leq 1$) upon Se Substitution. *Inorg. Chem.* **2018**, *57*, 13920–13928.

(45)   Shannon, R. D. Revised Effective Ionic Radii and Systematic Studies of Interatomie Distances in Halides and Chaleogenides Central Research and Development Department , Experimental Station , E . L Du Pont de Nemours The Effective Ionic Radii of Shannon & Prewitt [Acta. *Acta Cryst.* **1976**, *A 32*, 751–767.

(46)   Hanghofer, I.; Brinek, M.; Eisbacher, S. L.; Bitschnau, B.; Volck, M.; Hennige, V.; Hanzu, I.; Rettenwander, D.; Wilkening, M. Subsitutional Disorder: Structure and Ion Dynamics of the Argyrodites Li_6PS_5Cl, Li_6PS_5Br and Li_6PS_5I. *Phys. Chem. Chem. Phys.* **2019**, DOI: 10.1039/C9CP00664H.

(47)   Hoelzel, M.; Senyshyn, A.; Dolotko, O. SPODI: High Resolution Powder

Diffractometer. *J. large-scale Res. Facil. JLSRF* **2015**, *1*, 5.

(48) Hoelzel, M.; Senyshyn, A.; Juenke, N.; Boysen, H.; Schmahl, W.; Fuess, H. High-Resolution Neutron Powder Diffractometer SPODI at Research Reactor FRM II. *Nucl. Instruments Methods Phys. Res. Sect. A Accel. Spectrometers, Detect. Assoc. Equip.* **2012**, *667*, 32–37.

(49) Hoelzel, M.; Senyshyn, A.; Juenke, N.; Boysen, H.; Schmahl, W.; Fuess, H. High-Resolution Neutron Powder Diffractometer SPODI at Research Reactor FRM II. *Nucl. Instruments Methods Phys. Res. Sect. A Accel. Spectrometers, Detect. Assoc. Equip.* **2012**, *667*, 32–37.

(50) Coelho, A. A. TOPAS-Academic. *Coelho Software, Brisbane, Aust.* **2007**.

(51) Brug, G. J.; van den Eeden, A. L. G.; Sluyters-Rehbach, M.; Sluyters, J. H. The Analysis of Electrode Impedances Complicated by the Presence of a Constant Phase Element. *J. Electroanal. Chem.* **1984**, *176*, 275–295.

(52) Irvine, J. T. S.; Sinclair, D. C.; West, A. R. Electroceramics: Characterization by Impedance Spectroscopy. *Adv. Mater.* **1990**, *2*, 132–138.

For table of contents only